

LA-UR-00-3041

**Coordinated Observations of Optical Lightning from Space
Using the FORTE Photodiode Detector and CCD Imager**

D. M. Suszcynsky, T. E. Light

Los Alamos National Laboratory,

Space & Atmospheric Sciences Group, MS D466,

Los Alamos, NM 87545

S. Davis

University of Tulsa,

Dept. of Physics and Engineering Physics, 600 S. College,

Tulsa, OK 74104

J. L. Green, J. L. L. Guillen, W. Myre

Sandia National Laboratories,

Sensors and Electronics Dept., MS 0972,

Albuquerque, NM 87185

This paper presents an overview of the coordinated observation of optical lightning from space using the FORTE photodiode detector (PDD) and FORTE CCD imager also known as the Lightning Location System (LLS). PDD/LLS coincidence statistics are presented and show that both the detected energy density and detected peak irradiance of optical lightning events are proportional to the number of LLS pixels (pixel multiplicity) that are activated during the event. The inference is that LLS pixel multiplicity is more a function of the detected intensity and horizontal extent of the optical event rather than a direct indicator of the degree of scattering. PDD/LLS event coincidence is also used to improve upon traditional recurrence/clustering algorithms that discriminate against false LLS events due to energetic particles and glint. Energy density measurements of coincident events show that about 4 % of the optical energy detected by the broadband PDD appears in the narrowband LLS. This is in general agreement with ground-based measurements and with assumptions incorporated into the design of current and planned CCD imaging sensors.

1. INTRODUCTION

The satellite-based detection of optical emissions from lightning provides an effective way to monitor and study thunderstorm and lightning activity on a global basis. To date, two general types of optical detectors have been flown aboard satellites:

(1) photodiodes/photometers [e.g. *Vorpahl et al.*, 1970; *Sparrow and Ney*, 1971; *Turman*, 1977, 1978; *Turman and Tettelbach*, 1980; *Turman and Edgar*, 1982; *Orville and Henderson*, 1986; *Marshall et al.*, 1987; *Kirkland et al.*, 1998; *Suszcynsky et al.*, 1999, 2000] and (2) imagers [e.g. *Christian et al.*, 1999; *Boccippio et al.*, 1999; *Goodman et al.*, 2000; *Vonnegut et al.*, 1983], particularly those based on CCD-array technology.

Photodiodes and photometers are primarily utilized to provide time-resolved optical waveforms of lightning events. These waveforms reveal important information about the characteristics and phenomenology of individual lightning strokes and pulses [*Turman*,

1977, 1978; *Kirkland et al.*, 1998; *Suszcynsky et al.*, 1999, 2000], and the scattering effects of the intervening clouds [e.g. *Thomason and Krider*, 1982; *Kirkland et al.*, 1998; *Suszcynsky et al.*, 1999, 2000, *Light et al.*, 2000]. Photodiode/photometer systems are characterized by excellent temporal resolution (e.g. 10 – 100 μ s) and generally poor spatial resolution (100 - 1000 km).

Conversely, CCD imagers are primarily utilized to provide accurate geolocation and two-dimensional imagery of lightning events on flash timescales and are ideal for studying global and regional flash rates, and the diurnal, seasonal and geographical variations in lightning and storm activity [e.g. *Christian et al.*, 1999; *Goodman et al.*, 2000; *Boccippio et al.*, 1999]. CCD imager systems are characterized by excellent spatial resolution (1 – 10 km for low earth orbit platforms), low temporal resolution (1 – 10 ms), and a lack of waveform information.

This paper describes the phenomenology and analysis of optical lightning events that were simultaneously observed with both the

Photodiode Detector (PDD) and Lightning Location System (LLS) CCD imager aboard the Fast On-orbit Recording of Transient Events (FORTE) satellite. The high temporal resolution of the PDD ($\sim 15 \mu\text{s}$) and the high spatial resolution of the LLS imager ($\sim 10 \text{ km}$) combine to give a detailed satellite-based picture of both the spatial and temporal evolution of terrestrial lightning on both stroke (pulse) and flash timescales.

The goals of this study were to (1) present the basic phenomenology and techniques associated with the joint detection of optical lightning by a space-based photodiode sensor and CCD imager, (2) use the coordinated data set to explore the relationship between PDD optical waveform features and LLS pixel event characteristics, particularly as it pertains to the scattering of light by the intervening clouds, and (3) demonstrate the use of combined waveform/imager data to improve upon current satellite-based lightning data interpretation and discrimination techniques. After the introduction in this section, section 2 provides a brief description of the LLS and PDD instrumentation with

an emphasis on the LLS instrument. The results of the study are presented in section 3 and a discussion follows in section 4.

2. INSTRUMENTATION

2a. Description

The FORTE satellite was launched on August 29, 1997, into a nearly circular, 70°-inclination orbit of approximately 825-km altitude with an orbital period of about 100 minutes. The on-board instrumentation includes two broadband VHF receivers as described in *Jacobson et al.* [1999, 2000], the FORTE Photodiode Detector (PDD) as described by *Kirkland et al.* [1998] and *Suszcynsky et al.* [2000], and the FORTE Lightning Location Sensor (LLS) CCD imager which is detailed in this section. The PDD and the LLS are collectively referred to as the FORTE Optical Lightning System (OLS).

The PDD is a broadband (0.4 - 1.1 μm) silicon photodiode detector that collects amplitude versus time waveforms of lightning transients,

particularly those associated with individual strokes/pulses of a lightning flash. The instrument has an 80° field-of-view (FOV) which translates into a footprint of about 1200-km diameter for an 825-km altitude orbit. In the “autonomous” mode, the instrument produces 1.92 ms long waveforms with 15 μ s time resolution. Data collection is amplitude-threshold triggered, with a background-riding threshold, and with a requirement that the signal amplitude exceed the amplitude threshold for a pre-selected number of consecutive samples (typically five) before a trigger occurs. This protocol minimizes false triggers due to energetic particles. The instrument can also be run in a “slave” mode in which a 6.75 ms PDD record is collected in temporal coincidence with an LLS record whenever the LLS instrument triggers on an event. The PDD provides 12-bit sampling with a piece-wise linear dynamic range covering four orders of magnitude and a sensitivity of better than 10^{-5} W/m². The dead time between successive PDD records is approximately equal to the record length associated with the particular mode of operation. The trigger times of both the PDD and LLS records are GPS-time-stamped to a precision of 1 μ s.

The LLS is a CCD array that is optimally designed to identify and locate lightning flashes. The LLS instrument consists of a front-end optical assembly, a fixed-position CCD focal plane assembly with drive electronics and a Sandia-developed operations and signal processing module for lightning data discrimination. The front-end optical and CCD assemblies are identical to those used on the Lightning Imaging Sensor (LIS) developed by the National Aeronautics and Space Administration/Marshall Space Flight Center (NASA/MSFC).

The LLS optics consist of an f/1.6 tele-centric, multi-element focusing lens assembly with a 3.2 mm aperture and 5.3 mm focal length. The 80° x 80° square FOV approximately corresponds to that of the PDD and provides each pixel with a FOV of approximately 10 km x 10 km on the Earth's surface for an 825 km altitude. The narrow band spectral filter used in the lens assembly contains the OI(1) line at 777.4 nm which, according to previous ground-based studies, is a robust lightning emission line that contains ~ 1% of all emitted energy in the visible and

near-IR lightning spectrum (derived from data in *Orville and Henderson* [1984]). The filter is a multi-layer circular interference filter with a center wavelength (CWL) of 777.6 nm and a full-width half-maximum (FWHM) bandpass of 1.1 nm. It has a transmission of approximately 55 % in the passband and drops sharply to less than 7 % at $\text{CWL} \pm 2.2$ nm (Figure 1).

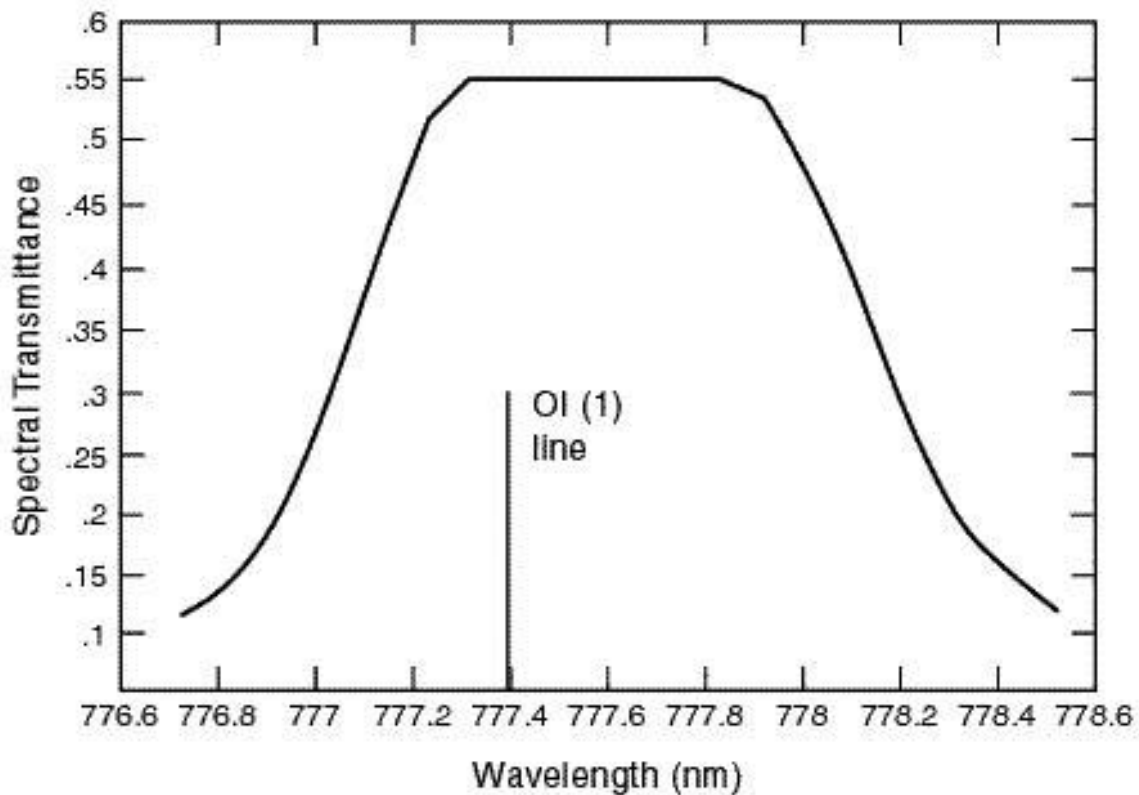


Figure 1

The focal plane array assembly consists of a 512 x 512 pixel ($15\mu\text{m}^2$ /pixel) CCD array and associated drive electronics. The total active

array size is 7.68 mm x 7.68 mm. Each image scene is integrated for 2.47 ms and results in a maximum frame rate of 405 frames/s. This frame integration time was selected to maximize lightning event detection and minimize event splitting between successive frames. After integration, the image frame is transferred (in ~ 10% of the frame integration time) to an internal non-imaging storage area on the array for processing, and a new frame of data begins to integrate. During this next frame integration period, the CCD array uses a 4 by 4 on-chip pixel binning operation (16 to 1) such that an effective array of 128 by 128 “macro” pixels (16384 total pixels) is created. A multiplexer is used to read out the macro pixels through four quadrant outputs and serially combines them into a single video channel. The single channel video output is a multiplexed sequence of data which begins with the pixel data of quadrant 1 and progresses through the data from quadrants 2, 3, and 4. The array macro pixels are read out from the quadrant corners in towards the center of the array.

The LLS operates autonomously with no external trigger capability. It is designed to operate in one of three internal trigger modes: normal (pixel event) mode, background (pixel event) mode and full frame (snapshot) mode. The normal (pixel event) mode and background (pixel event) mode are used to detect and locate lightning flashes to within a resolution of one pixel (~ 10 km) while the full frame mode is used for full frame imaging and diagnostics. When an LLS pixel event is detected, the LLS processing algorithm records the frame time of the event, and the address and amplitude for each pixel that participates in the pixel event. Because of the integrating nature of the LLS, the recorded pixel “amplitudes” are equivalent to energy densities.

In normal (pixel event) mode, a pixel event is declared when the pixel signal amplitude, I_S , for any given pixel exceeds the amplitude threshold level, I_T , for that pixel for less than three consecutive frame integration times. I_T is preset for each pixel by adding a commandable background trigger offset value to each individual pixel’s average background

amplitude, I_B . I_B is tracked with a background averaging algorithm and is calculated by

$$I_B = \frac{(\alpha - 1)I_{B,old}}{\alpha} + \frac{I_{B,new}}{\alpha} \quad (1)$$

where α is selectable as either 2, 4, 8 or 16 and governs how quickly the algorithm responds to changes in the background lighting. In this mode, only I_S is measured and known for each pixel. Consequently, the actual detected energy density of a lightning event cannot be deduced in this mode since I_S consists of both the detected energy density of the lightning event plus an additional unknown contribution due to noise and background.

The above process is performed at a rate of 8 million pixels/s which results in 125 ns of processing time per pixel. In that period of time, the digital circuitry calculates an updated value for I_B for each pixel, determines if a pixel event has occurred (if $I_S > I_T$ for any pixels), and

records data from any confirmed pixel event to an output FIFO for eventual transmission to the ground.

If $I_S > I_T$ for three or more consecutive frame integration times, the event is classified as glint and is discarded. Further triggering on each participating pixel is then disabled until I_S once again falls below the preset I_T . Glint events are most commonly generated from water or other terrestrial surfaces in the FOV or from the VHF antenna elements that lie within the FOV of the array. This algorithm removes a majority of, but not all, glint-related events.

Frame time for a pixel event is synchronized to the beginning of the event frame. When $I_S > I_T$ for two consecutive frame integration times, the actual event time recorded will correspond to the second frame time. If the rate of LLS pixel triggering exceeds a selectable maximum number of pixels per second (typically $\sim 400/\text{s}$), events will continue to be processed without being stored until the pixel rate drops back down below the maximum rate.

In background (pixel event) mode, the background tracking and thresholding is performed as described for the normal (pixel event) mode. However, in this mode the instrument also provides a reportable estimate of I_B for each pixel by collecting a subsequent frame of data immediately after the event frame. This is done by automatically switching to full frame mode (see next paragraph) at the end of the event frame, taking a scene snapshot, and then storing background data for only those pixels where I_S exceeded I_T in the original event frame. In principle, this measured value of I_B should very closely approximate the actual value of I_B that is calculated by equation 1 and used in the thresholding scheme. Once the background frame is collected, the instrument is switched back to pixel event mode to resume event monitoring. Although this mode is more processor and memory intensive than the normal mode, it reports actual values for both I_S and I_B , unlike the normal mode which just reports I_S . This mode is used to measure the actual detected energy density of lightning events.

During full frame mode, frame acquisition is controlled by the OLS micro-processor with a timed trigger method rather than by the threshold triggering scheme. In this mode, all 128 x 128 pixels (16384 total pixels/frame) are stored in event memory in 1K word quantities. A maximum of sixty-two frames can be stored in event memory with a maximum frame rate of 1 frame/s. Frame time is accurate to one second.

2b. Calibration

The amplitude calibration for the PDD was obtained prior to launch by measuring the responsivity of the PDD as a function of wavelength as it was illuminated by a calibrated benchtop source (Figure 2). Since the PDD responsivity is a function of wavelength and since the optical spectrum of lightning is somewhat variable from event to event, the PDD raw counts are typically converted to irradiances by using the average responsivity of the PDD over its entire spectral response. This average value of 0.3325 is shown as a dotted line in figure 2.

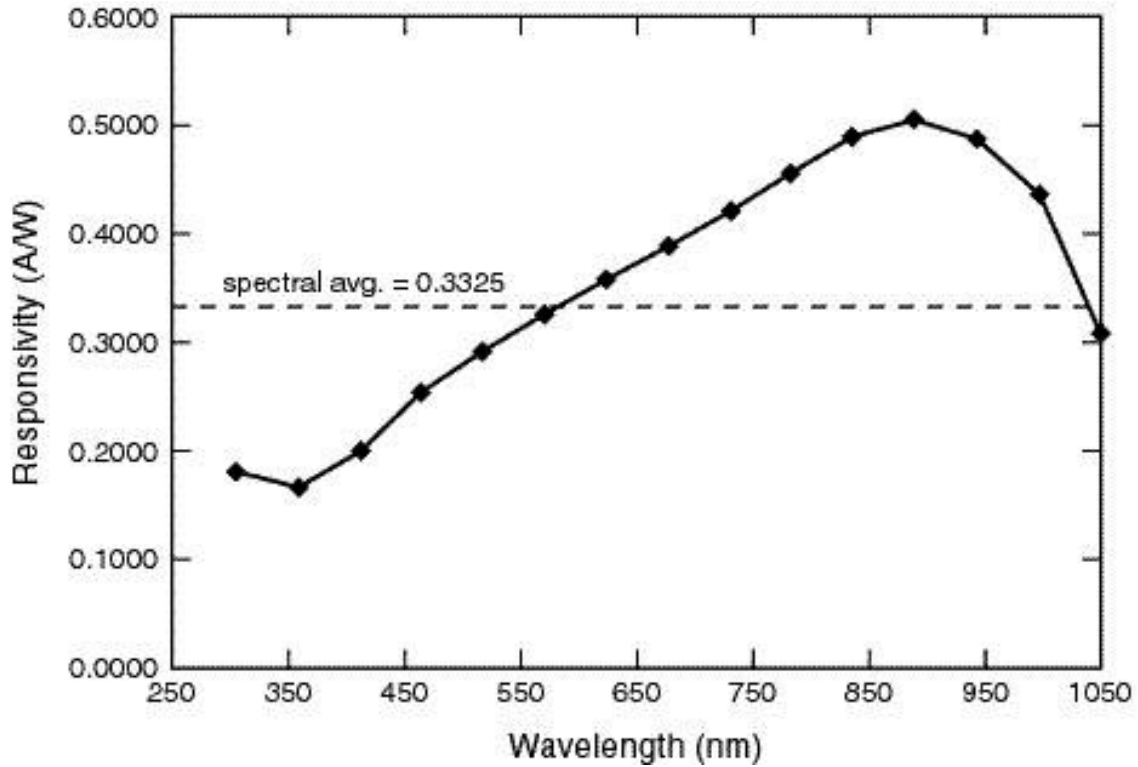


Figure 2

The pre-launch amplitude calibration for the LLS was problematic and was eventually repeated as a series of on-orbit calibrations by illuminating the satellite with a ground-based 330 mJ pulsed Alexandrite laser tuned and filtered to the passband of the LLS. The response of the LLS to the laser pulses was then cross-calibrated with the known calibration and response of the PDD. Figure 3 shows the results of this calibration and plots the LLS-detected energy density (E_{LLS}) of the on-orbit laser pulses versus the PDD-detected energy density (E_{PDD}) of those same pulses. A laser pulse within the passband of the LLS should

produce equal energy density measurements by both instruments (ie data should lie on the line $E_{LLS} = E_{PDD}$). Based on this technique, the amplitude calibration factor for the LLS was estimated to be $0.000028 \mu\text{J}/\text{m}^2/\text{count} \pm 12 \%$.

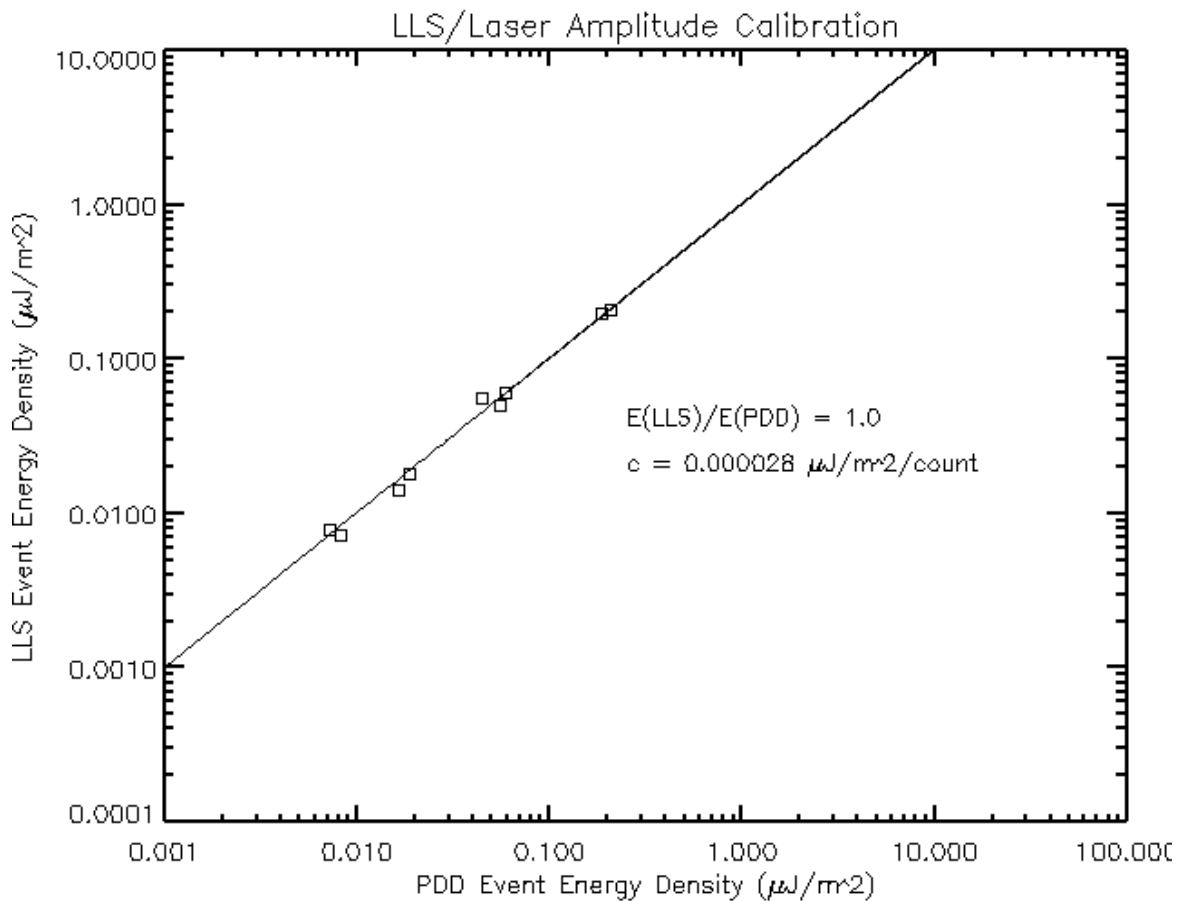


Figure 3

The laser calibrations were also used to fine-tune the LLS geolocation algorithm. Figure 4 shows a plot of 942 LLS-derived laser geolocations. The data is plotted as differences between the known

and measured geolocations of the laser in both latitude and longitude (in km). The laser was located at 35.052 N and 106.535 W and was geolocated in nearly all cases, to within an uncertainty of one pixel (~ 10 km). The circular error probable (CEP), that is, the radius of the circle about the known laser location that encompasses 50% of the points is about 5.1 km.

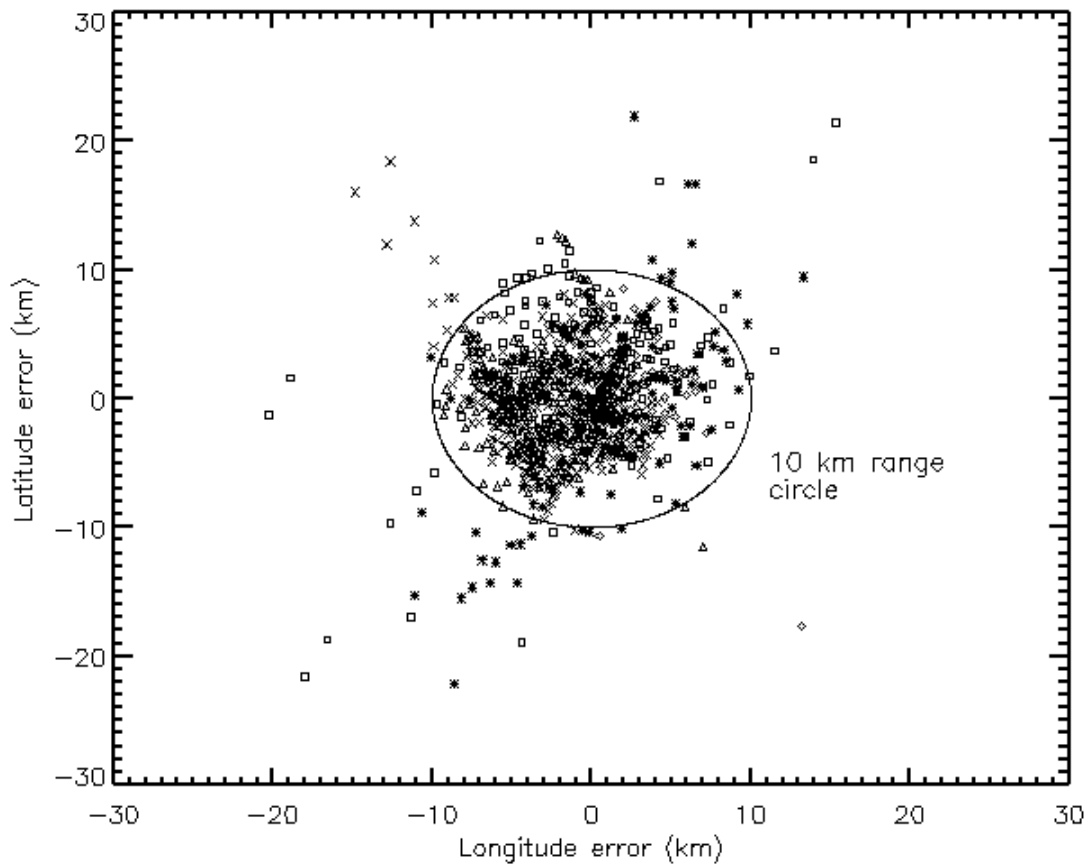


Figure 4

3. OBSERVATIONS AND ANALYSIS TECHNIQUES

3a. PDD/LLS Correlations

As a sensor suite, the PDD and LLS sensors are operated in either the autonomous or slaved mode. Each mode has its advantages in certain situations. In the autonomous mode, each instrument is operated independently from the other and is subjected to its own set of triggering and sensitivity biases. When a storm is in the sensors' FOV, the correlation rate, that is, the percentage of lightning triggers in one instrument that are in temporal coincidence with lightning triggers from the other instrument, is quite variable and can range anywhere from around 50 % down to much less than 1 %. In this mode, the correlation rate is a sensitive function of the triggering and sensitivity thresholds for each instrument, local time, geographic position, and storm characteristics. The autonomous mode is most often used for PDD global lightning surveys and data collection in the SAA and auroral zones where the high rate of LLS false triggers due to energetic particles makes it impractical to slave the PDD to the LLS.

In the slave mode, as previously described, PDD triggers are forced whenever an LLS trigger occurs, thereby eliminating the triggering and sensitivity biases of the PDD. When the instruments are operated in this mode at night (similar sensitivities) and in geographic regions away from the penetrating effects of energetic particles associated with the SAA and auroral zones, the correlation rate between LLS and PDD lightning detections is better than 95%. This is generally the preferred mode of operation for high temporal and spatial resolution measurements and studies of lightning at both the stroke and flash level since it guarantees a geolocation for each collected PDD lightning trigger.

Regardless of which mode is used, the correlation rate between the LLS and the PDD lightning triggers is generally much higher than previous FORTE correlation studies

(e.g. FORTE/VHF versus NLDN/VLF [*Jacobson et al.*, 2000], FORTE/VHF versus FORTE/PDD [*Suszcynsky et al.*, 1999, 2000])

and FORTE/PDD versus NLDN/VLF [*Suszcynsky et al.*, 1999]), primarily because the PDD and LLS detect the same type of radiation.

3b. General Statistics

Figures 5-10 illustrate some of the fundamental statistical properties of the coordinated PDD/LLS data set. All data was collected in the autonomous mode during night time conditions (roughly equal LLS and PDD sensitivities) in the October 1, 1998 to April 1, 1999 time interval. The LLS was operated in the background (pixel event) mode with an $I_T \sim 0.00070 \mu\text{J}/\text{m}^2$ (25/4096 ADC counts). The correlated data set was filtered to eliminate LLS events that (1) triggered in regions of the array where the RF antenna/boom might obscure portions of an event (i.e. part of the emitted energy), and (2) contained saturated pixels indicative of glint/reflection events.

Figure 5 shows a histogram of the number of pixels activated per LLS pixel event (i.e. pixel multiplicity) for 38999 lightning events simultaneously detected by both the LLS and PDD. The data was selected by requiring that each LLS event be accompanied by a non-noise and non-particle-induced PDD event (i.e. lightning), and that the PDD event occur some time during the 2.5 ms integration time of the LLS record. The requirement that the LLS trigger be in temporal coincidence with a PDD trigger virtually eliminates false LLS triggers due to energetic particles or glint. This point is further discussed in section 4. The distribution in Figure 5 indicates that approximately one-third of joint LLS/PDD-detected lightning events are one-pixel events while 97 % of the LLS events contain 10 or fewer pixels. This result is somewhat different from that obtained by considering the population of all LLS events (regardless of PDD coincidence), for which the majority are energetic particle events. In this case, about two-thirds of the LLS events are one-pixel events with 98% of the events containing 10 or fewer pixels.

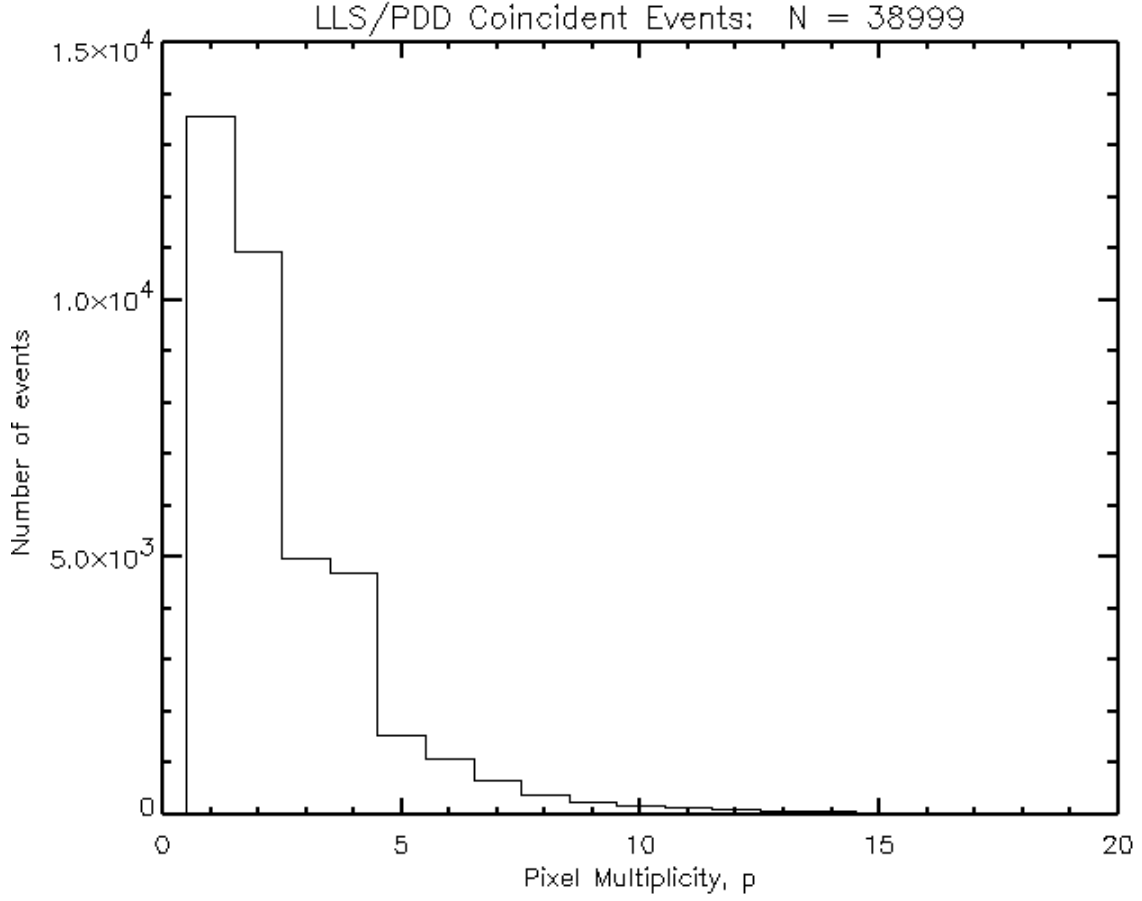


Figure 5

Figure 6 plots the LLS-measured (asterisks) and PDD-measured (crosses) mean optical energy densities of the lightning events in Figure 5 as a function of the pixel multiplicity. The mean LLS event energy density, \overline{E}_{LLS} , for a given pixel multiplicity, p , was calculated as

$$\overline{E}_{LLS}(p) = \frac{1}{n_p} \sum_{j=1}^{n_p} \sum_i (I_{s,i,j} - I_{b,i,j}) / n_p \quad (2)$$

where n_p is the total number of events with a given p , and $I_{s,i,j}$ and $I_{b,i,j}$ are the detected signal and background energy densities for the i th pixel in the j th pixel event. The mean PDD event energy densities, $\bar{\mu}_{PDD}$, were calculated by averaging the integrated PDD waveforms. Values for n_p are indicated along the abscissa below each data point. The data is plotted only for $p \leq 10$ because memory limitations for the current LLS database restrict database entries to a 10-pixel limit. On the average, the detected energy densities of both the LLS and PDD events increase with p . The difference in the detected mean energy densities between the PDD and LLS data is consistent with the fact that the PDD covers a broader spectral range than the LLS. This point is more directly addressed in Figure 10 and section 4.

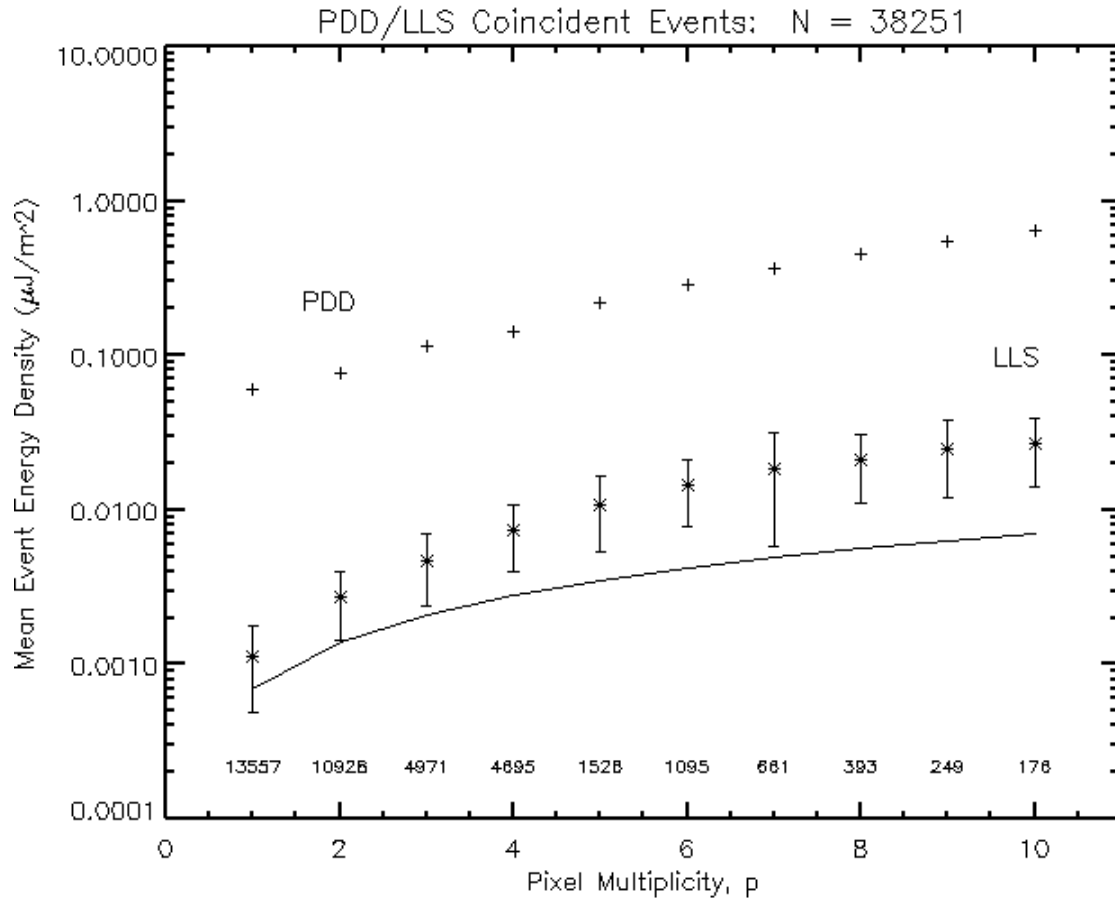


Figure 6

The trend in figure 6 is apparently a valid relationship between the detected mean optical energy density of a lightning event and the corresponding LLS pixel multiplicity and is not a thresholding or pixel saturation effect. The vertical bars on the LLS data points in figure 6 span plus and minus one standard deviation (± 1) about each mean and lie significantly above the solid line that represents the minimum detectable energy density for each pixel multiplicity. The minimum

detectable LLS event energy density, $E_{LLS,min}$, as a function of p , is given by $E_{LLS,min}(p)=p*c*25$ where $c=0.000028 \mu\text{J}/\text{m}^2/\text{count}$ and where it is assumed that $I_B = 0$. Since I_B is generally not zero, this line represents an upper limit to $E_{LLS,min}$. Consequently, the trend does not seem to be driven by detection threshold issues. Likewise, there is no indication of a saturation effect in the data. Figure 7 shows energy histograms for selected pixel multiplicities ($p = 1, 4, 7$) in Figure 6. The distributions are well-behaved and show no indication of an abrupt upper limit cutoff that might be indicative of a pixel saturation effect that could lead to blooming (artificial increase in p). Distributions for each of the remaining pixel multiplicity bins are equally well-behaved.

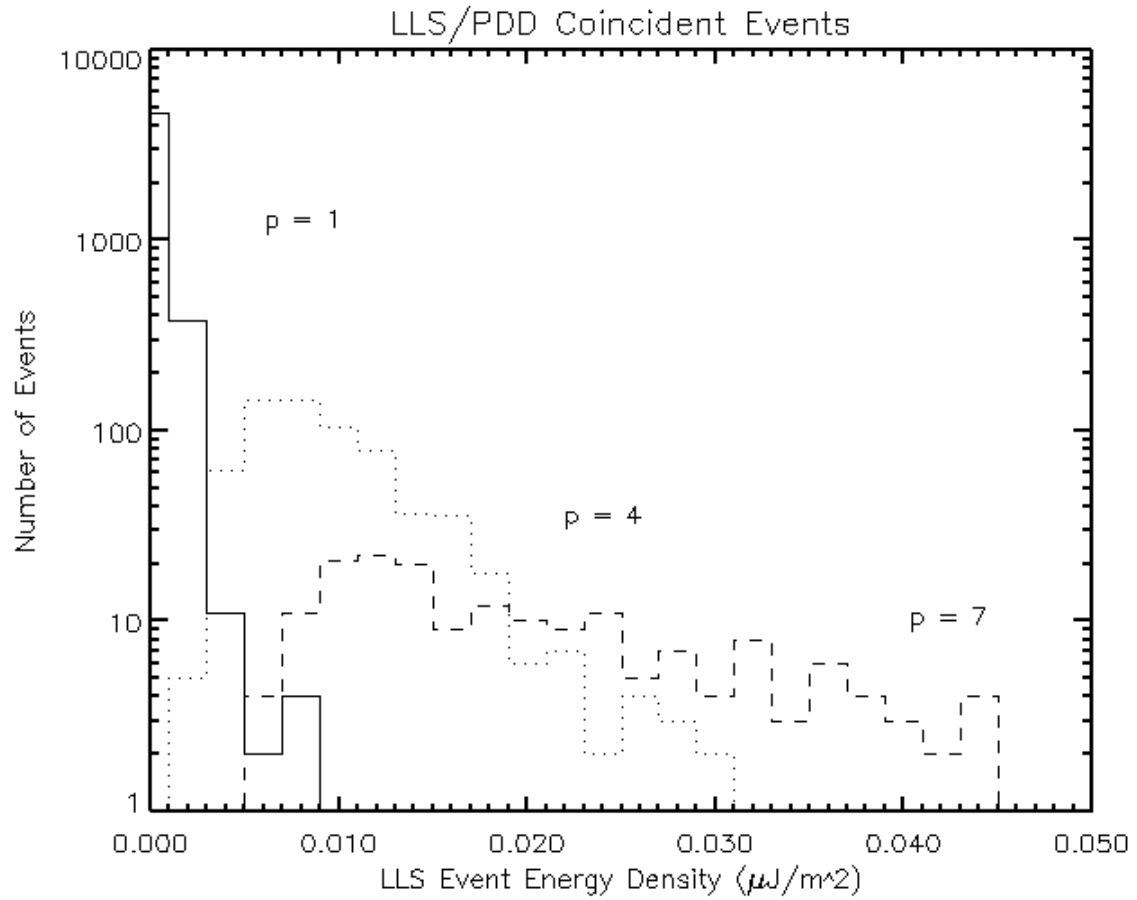


Figure 7

Figure 8 illustrates the mean peak irradiance in W/m^2 for the pixel events shown in figure 5. The mean peak irradiances for the events are

proportional to the pixel multiplicity.

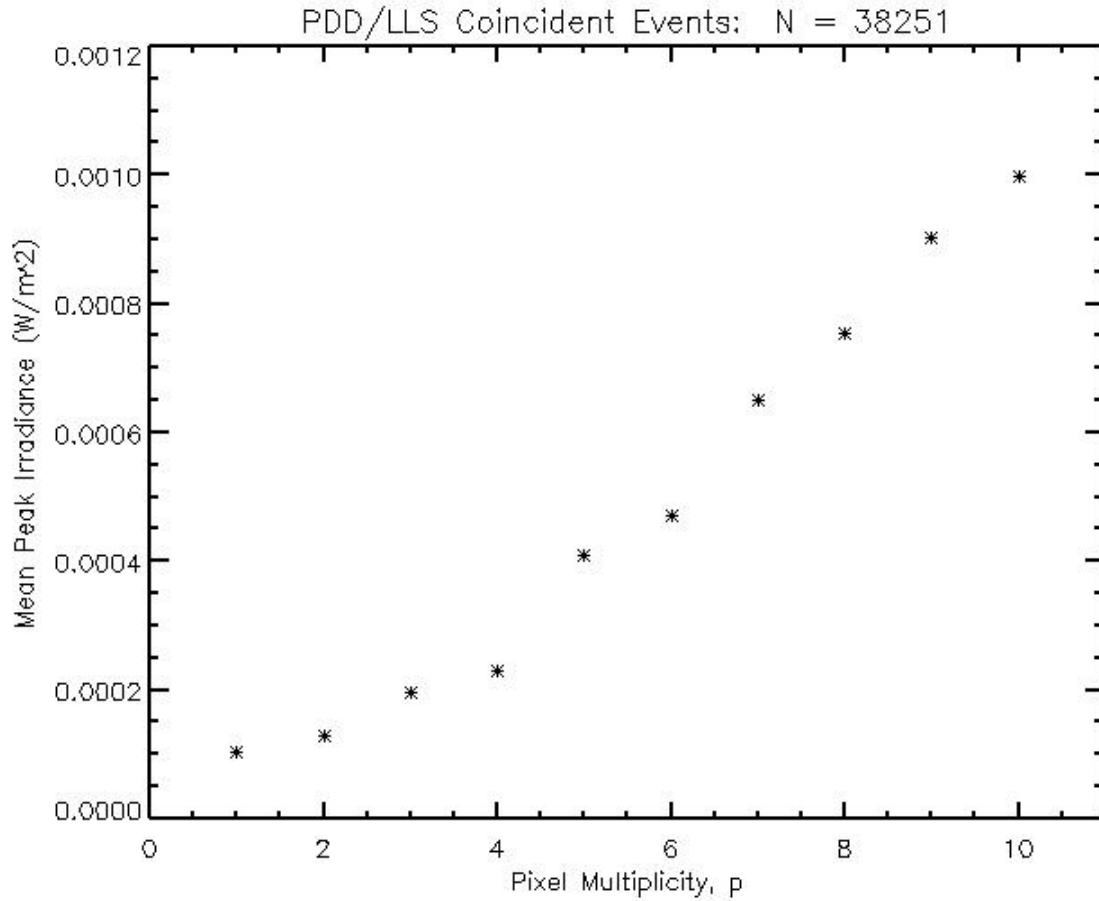


Figure 8

Figure 9 plots the effective pulse width in seconds for the events in figure 5 as a function of pixel multiplicity. The effective pulse width is defined as the pulse energy divided by the peak irradiance [Mackerras, 1973] and is independent of the number of pixels per event. The mean widths for each p value are indicated by asterisks and the median widths are represented as

diamonds.

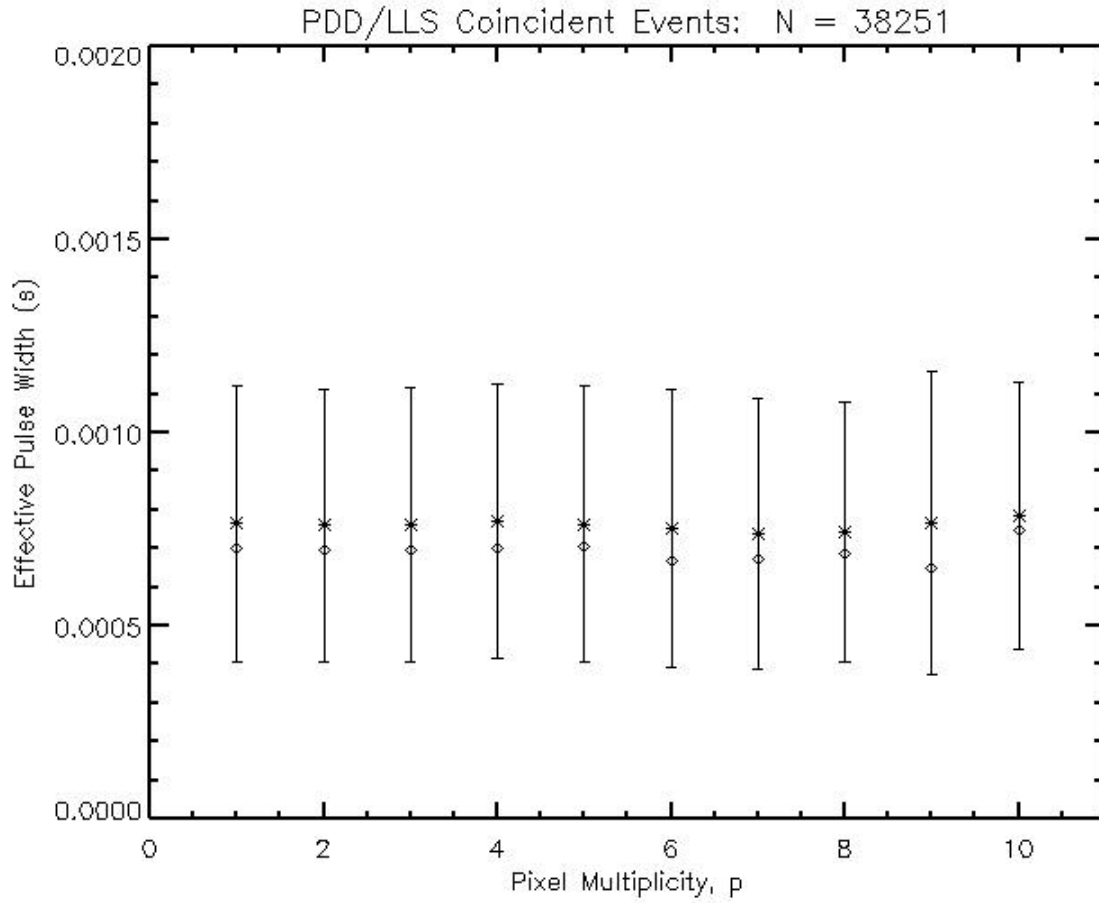


Figure 9

Figure 10 details the relationship between the LLS-derived energy density (E_{LLS}) and the PDD-derived energy density (E_{PDD}) for the events in Figure 5. The E_{LLS} values for each pixel event were calculated by subtracting I_B from I_S and then summing this difference over all pixels participating in the pixel event. The best-fit line through the data is given

by $E_{\text{LLS}} = 0.04 E_{\text{PDD}}$ and is a least-squares fit that is forced through the origin. The fairly abrupt cutoff of data points below $E_{\text{LLS}} \sim 0.00070 \mu\text{J}/\text{m}^2$ represents the trigger threshold of the LLS instrument (25 out of 4096 amplitude counts). Some data lie below this level as a consequence of (1) the limiting inaccuracies of the background determinations for low signal-to-noise events, and (2) the fact that some background measurements occur during on-going lightning activity, and consequently overestimate the background. Lightning contaminated background measurements occur no more than about 5-10% of the time.

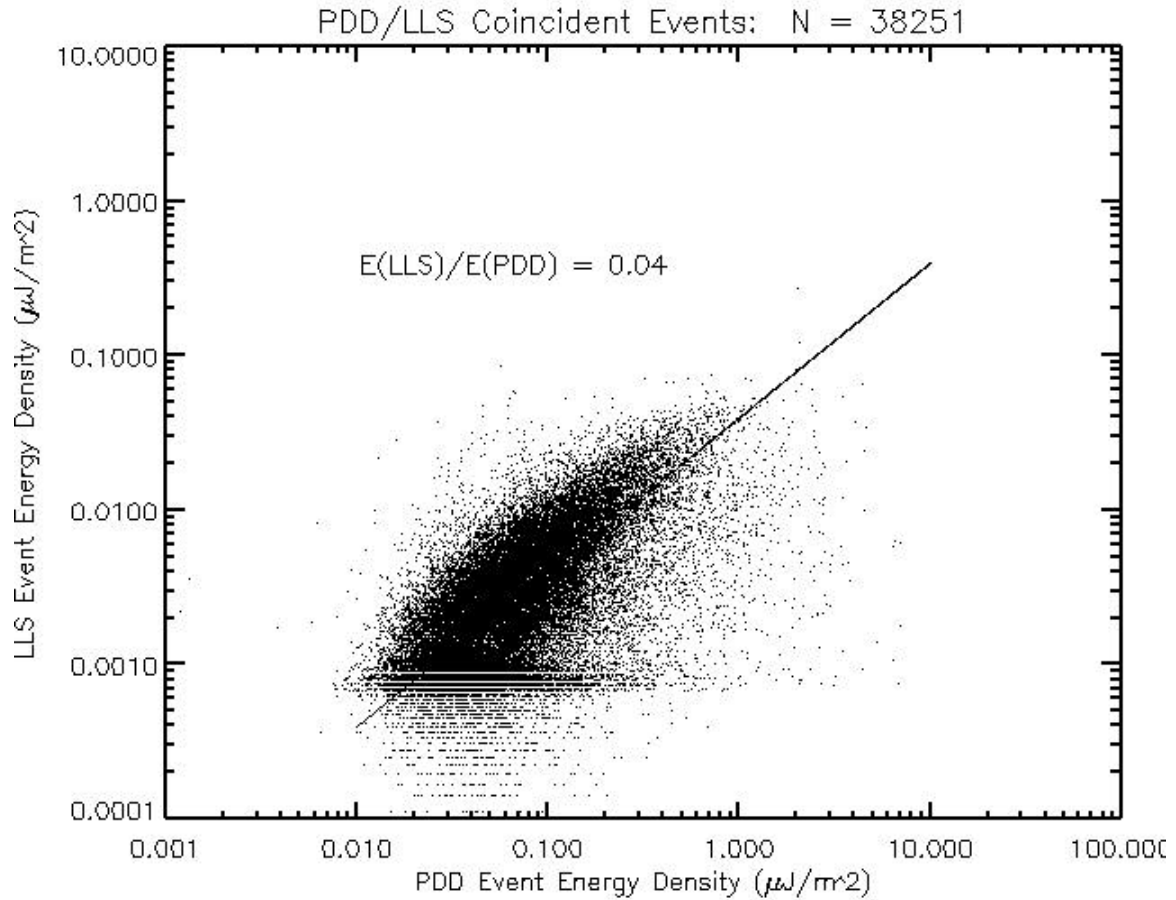


Figure 10

3c. Data Discrimination Techniques

A fundamental challenge in the analysis of lightning data collected by satellite-based CCD arrays is to effectively discriminate between true lightning events and unwanted energetic particle/glint events. For the FORTE/LLS data set, some of this discrimination is performed by (1) discarding pixel events that contain saturated pixels (usually due to glint

or excessive reflections off clouds or other objects in the near and far field), and (2) discarding events that are comprised solely of pixels known to be obscured by the VHF antenna or other spacecraft components in the LLS FOV. However, the bulk of our discrimination capability makes use of the known temporal and spatial characteristics of lightning.

NASA/MSFC, as part of its Optical Transient Detector (OTD) and Lightning Imaging Sensor (LIS) satellite sensor programs, has pioneered various data discrimination methods for CCD-array lightning detection based on a “validation by association” technique. These data “clustering” techniques effectively validate lightning events by identifying recurrent spatial and temporal patterns in the lightning activity [e.g. *Mach et al.*, 1999].

The basic FORTE/LLS data discrimination technique is based on a modified clustering algorithm that is built around PDD/LLS coincident data rather than just the LLS data alone. Under certain conditions, this

addition of PDD photodiode data can significantly improve upon discrimination results obtained with just imager data. A simple example of such an instance is shown in Figure 11.

Figure 11a shows raw LLS-geolocated events (yellow crosses) from an ascending pass over the southern tip of Africa from 18:29 UT to 18:34 UT on July 21, 1998. Two types of LLS events are apparent: (1) ubiquitous events that are fairly evenly distributed geographically and are predominantly due to energetic particles associated with the easternmost extent of the SAA, and (2) localized accumulations of events (e.g. southwest of Madagascar and to the east of the tip of Africa) that are presumably due to recurrent lightning activity. The events are superimposed on a visible-light satellite image that was taken at 18:00 UT, 30 minutes before the pass.

Figure 11b illustrates the limitations in applying a pure LLS clustering algorithm to the data in figure 11a. Figure 11b plots only those LLS events that are most likely associated with recurrent storm emission, in

other words, those that occur within x kilometers and t seconds of each other. Typically, t is chosen to be on the order of the satellite pass time (~ 200 s for storms lying in the center of the LLS FOV) and x is chosen to be large enough so that it maximizes recovery of valid lightning events associated with the same storm complex, but not so large that it begins to incorporate lightning events from other storm systems or a significant number of particle events. For mid-latitude storms away from the SAA and auroral zones, x is typically ~ 100 km. However, in high energetic particle rate environments, the value of x must be reduced. For the data illustrated in Figure 11b, x was chosen to be 10 km, the resolution of the imager. In spite of this exceptionally low value for x , the algorithm still clusters some particle events and incorrectly identifies them as valid lightning events. This is most clearly seen to the west of Madagascar where the algorithm produces “valid” lightning events over a region that is clearly devoid of clouds.

Figure 11c illustrates how coincident PDD data can be used to improve discrimination capability in high background environments such as is

shown in figure 11a. In figure 11c, we first identify valid LLS lightning events (red crosses) by only considering those LLS events that are in temporal coincidence with a PDD event (PDD event time occurs within the 2.5 ms integration time of the LLS frame). This virtually eliminates any possibility that the LLS event was particle-induced. We then add to that LLS population any additional LLS events that occur within x kilometers of any of those events (yellow crosses). The value for x is chosen as previously described ($x = 100$ km for figure 11c). As can be seen in figure 11c, this modified clustering technique effectively identifies the lightning producing regions associated with cloud cover, while effectively discarding those temporally and spatially clustered events to the west of Madagascar that are clearly associated with the SAA rather than convective storm activity.

The LLS and PDD data sets displayed in figure 11 were each collected autonomously. When the instruments are operated in the slave mode, event discrimination can be even more directly applied by simply noting whether the PDD waveform is particle-like or lightning-like.

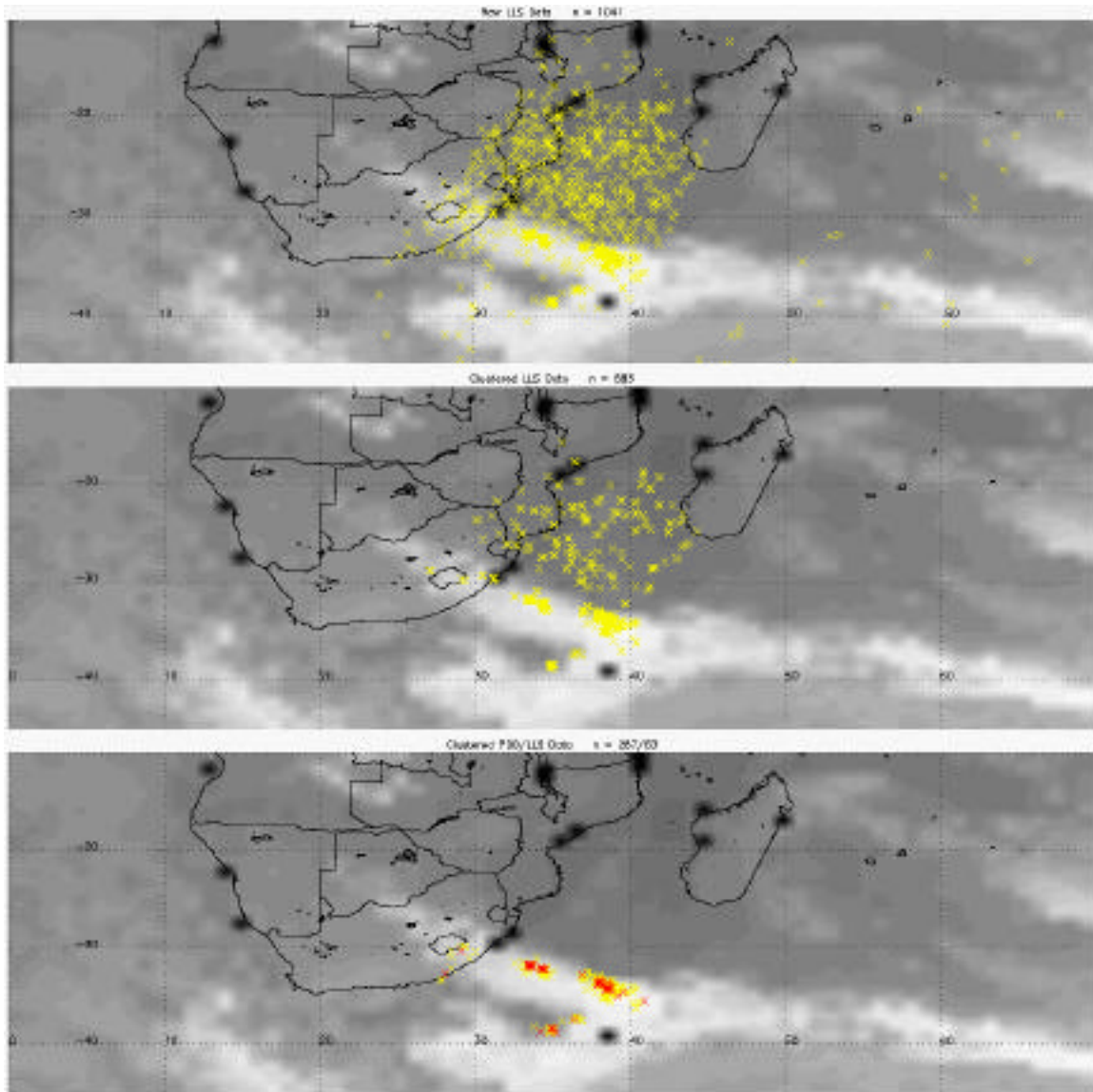


Figure 11

4. DISCUSSION

While it is clear that the results of figures 5-10 cannot be used to predict details of the source function (lightning) and the transfer function (cloud characteristics) on a case by case basis, the results can be used to explore the statistical relationship between waveform features and pixel

event characteristics. The study of these relationships is particularly applicable to the statistical interpretation of current and future CCD imager data for which photodiode data is not or would not be available. The comparisons also allow us to make general inferences as to the relative contributions of event intensity and scattering to the PDD waveform and LLS pixel characteristics.

As shown in figure 5, approximately one-third of LLS pixel events are comprised of one pixel. However the majority of LLS events span two or more pixels. This pixel multiplicity is a function of several inter-related factors. Clearly, a pixel will not be triggered unless the optical energy falling upon it exceeds the LLS trigger threshold criteria for that pixel. The amount of optical energy intercepted by a given pixel is dependent upon the strength of the source, the geometric orientation of the source with respect to the satellite direction, and the amount of scattering, absorption and reflection that the emitted light experiences during its path through the cloud to the satellite.

It is important here to distinguish between the source intensity of an event and its intensity as detected by the satellite. The source intensity refers to the intrinsic optical energy density of an event at its source. The detected intensity refers to the detected optical energy density at the satellite and differs from the source intensity because of the scattering and absorptive effects of the intervening cloud. Although the degree of scattering must contribute somewhat to the total number of pixels that are activated during a pixel event, it will be argued below that, in general, pixel multiplicity is primarily driven by the detected intensity of the optical event and its horizontal extent with respect to the source-satellite line-of-sight.

The above generalization is based on several observations. First of all, figure 6 shows a strong increase in the mean detected event energy density as a function of pixel multiplicity. It is difficult to explain this trend with a scattering argument, since on the average, scattering would tend to conserve or even reduce the total detected energy density in a given pixel event rather than increase it. One would expect the curve in

figure 6 to have a zero or negative slope in this case. The same can be argued for the peak irradiance in figure 8. A scattering explanation would argue for a flat or even decreasing average peak irradiance as a function of the number of pixels per event.

This interpretation is further supported by the results of figure 9 which show no indication of a pixel-multiplicity dependence on pulse width. If the pixel multiplicity was primarily related to the degree of scattering, we would expect to see an increase in the mean pulse width as a function of pixel multiplicity. Most light transmission models [e.g. *Thomason and Krider*, 1982; *Koshak et al.*, 1994; *Light et al.*, 2000] and data [e.g. *Goodman et al.*, 1988; *Suszcynsky et al.*, 2000] suggest optical pulse broadening of a few to several hundred μs for the densest clouds. Such a broadening is within one standard deviation of the calculated means over the pixel multiplicity range of 1 to 10. However, taken together with figures 6 and 8, the results strongly imply that large pixel multiplicity LLS events are generally a result of larger detected optical intensities

and/or more spatially extended events rather than simply a result of scattering.

Finally, figure 10 presents an in-situ measurement of E_{LLS}/E_{PDD} for 38251 events. Since the LLS is filtered to a 1 nm bandpass centered on the 777.4 nm line, this ratio basically measures the fractional contribution of the optical output of the OI(1) line to that of the entire visible and near-IR part of the spectrum (the 400 – 1100 nm bandpass of the PDD). An in-situ measurement of this number is useful because (1) it validates and quantifies the choice of the OI(1) line as a robust emission line for space-based detection of lightning and (2) it provides a large statistical ensemble of measurements that can be used to define the natural variability of the lightning spectrum. This ratio is estimated to be about 0.01 based on the limited ground data of *Orville and Henderson* [1984] (10 return strokes) and is measured at ~ 0.04 from the data in figure 10.

The FORTE-measured ratio has an inherent error in that the spectral dependence of the PDD calibration factor is approximated as a constant (0.3325 A/W at 580 nm, see figure 2). However, the actual PDD spectral response was convolved with a typical representation of a lightning spectrum from *Orville and Henderson* [1984] and the resulting energy ratio was found to differ from that derived with the constant calibration factor by only a few percent. Consequently, the error introduced into the ratio measurement by assuming a constant PDD response should be small compared to the observed order of magnitude variation in E_{PDD} for a given E_{LLS} .

A second source of error is that the PDD has a small but finite spectral response outside the 380 – 900 nm passband of the *Orville and Henderson* [1984] results (figure 2). However, optical radiation below a wavelength of 380 nm would not reach the satellite because of the scattering effects of the atmosphere. On the other hand, radiation in the 900 – 1100 nm wavelength range (the spectral range covered by the PDD and not measured by *Orville and Henderson* [1984] is detected

by the PDD and would result in a slight under-estimation of the ratio as compared to the *Orville and Henderson* [1984] value of 0.01. In summary, the results of this study estimate the ratio to be at least a factor of 4 greater than that inferred from the *Orville and Henderson* [1984] data. This discrepancy may be related to the fact that *Orville and Henderson* [1984] considered only return strokes while the FORTE data set is dominated by in-cloud events [*Suszcynsky et al.*, 1999].

A natural variability in the ratio is hinted at in the 10 examples studied in figure 5a,b of *Orville and Henderson* [1984], but this variability is obvious in the order of magnitude spread shown for the 38251 events of figure 10. Some of this spread can be attributed to lightning-contaminated background measurements (~ 5 - 10% of the cases). However, the majority of the spread is apparently a result of the natural variability of the spectral output of lightning as seen from space. This variability is a likely function of lightning type, the altitude of the source emission, and the degree of wavelength-dependent

scattering and absorption in the cloud. Instrumental contributions to the variability are minimal. The calibration data of figure 3 shows that the ratio should be stable to within about $\pm 10\%$ for a constant source spectrum. In addition, there is no evidence that the variability is a function of the magnitude of the detected energy density or detected peak irradiance.

In summary, the OI(1) line is a well-chosen line for the space-based detection of lightning in that it reliably produces $\sim 4\%$ of the light available in the visible and near IR region of the spectrum. However, the natural variability of the lightning spectrum precludes the use of this line as an accurate proxy to estimate the total available optical energy density in the visible/near IR portion of the spectrum to better than an order of magnitude.

ACKNOWLEDGEMENTS

The authors would like to thank Dick Spalding and Roman Martinez of Sandia National Laboratories, Matt Kirkland, Abe Jacobson, Phil Klingner and Bob Franz of Los Alamos National Laboratory and the rest of the FORTE Science and Operations Teams for essential discussions, comments, and support during this study. This work was supported by the United States Department of Energy.

REFERENCES

Boccippio, D. J., W. J. Koshak, H. J. Christian, and S. J. Goodman, Land-ocean differences in LIS and OTD tropical lightning observations, *Proceedings of the 11th International Conference on Atmospheric Electricity*, H. Christian (ed.), NASA/CP-1999-209261, 734-737, 1999.

Christian, H. J., R. J. Blakeslee, D. J. Boccippio, W. L. Boeck, D. E. Buechler, K. T. Driscoll, S. J. Goodman, J. M. Hall, W. J. Koshak, D. M. Mach, and M. F. Stewart, Global frequency and distribution of lightning as observed by the optical transient detector (OTD) , *Proceedings of the 11th International Conference on Atmospheric Electricity*, H. Christian (ed.), NASA/CP-1999-209261, 726-729, 1999.

Goodman, S. J., H. J. Christian, and W. D. Rust, A comparison of the optical pulse characteristics of intracloud and cloud-to-ground lightning as observed above clouds, *J. Applied Meteor.*, 27, 1369-1381, 1988.

Goodman, S. J, D. E. Buechler, K. Knupp, K. Driscoll, and E. W. McCaul, Jr., The 1997-98 el nino event and related wintertime lightning variations in the southeastern united states, *Geophys. Res. Lett.*, 27, 541-544, 2000.

Jacobson, A. R., S. O. Knox, R. Franz, D. C. Enemark, FORTE observations of lightning radio-frequency signatures: capabilities and basic results, *Radio Sci.*, 34, 337-354, 1999.

Jacobson, A. R., K. L. Cummins, M. Carter, P. Klingner, D. Roussel-Dupre, S. O. Knox, FORTE radio-frequency observations of lightning strokes detected by the National Lightning Detection Network, *J. Geophys. Res. – Atmos.*, 105, 15653-, 2000.

Kirkland, M. W., D. M. Suszcynsky, R. Franz, J. L. L. Guillen, J. L. Green, Observations of terrestrial lightning at optical wavelengths by the photodiode detector on the FORTE satellite, Rep. LA-UR-98-4098, Los Alamos Natl. Lab., Los Alamos, N. M., 1998.

Koshak, W. J., R. J. Solakiewicz, D. D. Phanord, and R. J. Blakeslee, Diffusion model for lightning radiative transfer, *J. Geophys. Res. – Atmos.*, 99, 14361-14371, 1994.

Light, T. E., D. M. Suszcynsky, M. W. Kirkland, and A. R. Jacobson, Simulations of lightning optical waveforms as seen through clouds by satellites, submitted to *J. Geophys. Res. – Atmos.*, 2000.

Mach, D. M., W. Boeck, and H. Christian, An intercomparison of ground, airborne, and space instrumentation definitions of the lightning element, *Proceedings of the 11th International Conference on Atmospheric Electricity*, H. Christian (ed.), NASA/CP-1999-209261, 166-169, 1999.

Mackerras, D., Photoelectric observations of the light emitted by lightning flashes, *J. Atmos. Terr. Physics*, 35, 521-535, 1973.

Marshall, J. D., S. C. Fox, N. K. Blocker, and B. N. Turman, A GPS/NDS lightning study, Rep. AFTAC-TR-87-1, Air Force Technical Applications Center, Patrick Air Force Base, Florida, 1987.

Orville, R. E. and R. W. Henderson, Absolute Spectral Irradiance Measurements of Lightning from 375 to 880 nm, *J. Atmos. Sci.*, 41, 3180-3187, 1984.

Orville, R. E. and R. W. Henderson, Global Distribution of Midnight Lightning: September 1977 to August 1978, *Mon. Wea. Rev.*, 114, 2640-2653, 1986.

Sparrow, J. G. and E. P. Ney, Lightning observations by satellite, *Nature*, 232, 540-541, 1971.

Suszcynsky, D. M., M. Kirkland, P. Argo, R. Franz, A. Jacobson, S. Knox, J. Guillen, J. Green, and R. Spalding, Thunderstorm and Lightning Studies Using the FORTE Optical Lightning System (FORTE/OLS), *Proceedings of the 11th International Conference on Atmospheric Electricity*, H. Christian (ed.), NASA/CP-1999-209261, 672-675, 1999.

Suszcynsky, D. M., M. W. Kirkland, A. Jacobson, R. Franz, S. Knox, J. L. Guillen, J. Green, FORTE Observations of Simultaneous RF and Optical Emissions from Lightning: Basic Phenomenology, *J. Geophys. Res. - Atmos.*, *105*, 2191-2201, 2000.

Thomason, L. W. and E. P. Krider, The effects of clouds on the light produced by lightning, *J. Atmosph. Sci.*, *39*, 2051-2065, 1982.

Turman, B. N., Detection of lightning superbolts, *J. Geophys. Res.*, *82*, 2566-2568, 1977.

Turman, B. N., Analysis of lightning data from the DMSP satellite, *J. Geophys. Res.*, 83, 5019-5024, 1978.

Turman, B. N. and B. C. Edgar, Global lightning distributions at dawn and dusk, *J. Geophys. Res.*, 87, 1191-1206, 1982.

Turman, B. N. and R. J. Tettelbach, Synoptic-scale satellite Observations in conjunction with tornadoes, *Mon. Wea. Rev.*, 108, 1878-1882, 1980.

Vonnegut, B., O. H. Vaughan, and M. Brook, Photographs of lightning from the space shuttle, *Bull. Amer. Met. Soc.*, 64, 150-151, 1983.

Vorpahl, J. A., J. G. Sparrow, and E. P. Ney, Satellite observations of lightning, *Science*, 169, 860-862, 1970.

FIGURE CAPTIONS

Figure 1. Spectral transmittance of the LLS filter as a function of wavelength.

Figure 2. Responsivity of the PDD as a function of wavelength.

Figure 3. LLS-measured energy density versus PDD-measured energy density for the in-situ LLS/laser amplitude calibration . Solid line represents a least-squares fit of the data using a calibration constant of $0.000028 \mu\text{J}/\text{m}^2/\text{count}$.

Figure 4 LLS geolocation errors plotted as differences between the known and measured latitude and longitude of a ground-based laser. Data collected Dec. 12, 1998 (), Oct. 15, 1998 (), Oct. 16, 1998 (*), Nov. 20, 1999 (), and Nov. 21, 1999 (x).

Figure 5 Histogram of the LLS pixel multiplicity for 38999 lightning events simultaneously detected by the PDD and LLS.

Figure 6 LLS-measured (*) and PDD-measured (+) mean optical energy densities as a function of pixel multiplicity for the lightning events in figure 5. The vertical bars represent ± 1 about the means and the solid line represents the minimum detectable energy density for a given pixel multiplicity.

Figure 7 Histogram of energy densities for selected pixel multiplicities ($p = 1, 4, 7$) of the data in figure 6.

Figure 8 Mean peak irradiance in W/m^2 as a function of pixel multiplicity for the lightning events in figure 5.

Figure 9 The mean (*) and median () PDD-measured effective pulse widths as a function of pixel multiplicity for the lightning events in figure 5. The vertical bars represent ± 1 about the mean values.

Figure 10 LLS-measured energy density versus PDD-measured energy density for the lightning events in figure 5. Solid line represents a least-squares fit of the data forced through the origin.

Figure 11 (a) 1041 “raw” LLS-geolocated lightning events (yellow x’s) from 18:29 UT to 18:34 UT on July 21, 1998, (b) The subset of 583 “true” lightning events (yellow x’s) as identified by the conventional clustering algorithm described in the text, $x = 10$ km. (c) The subset of 287 “true” lightning events as identified by the modified clustering algorithm described in the text. Red x’s represent the 63 events detected by both the PDD and LLS; yellow x’s represent the 224 additional events detected by the LLS and within $x = 100$ km of the PDD/LLS pairs of data. The results in (a), (b), and (c) are each superimposed on visible satellite imagery taken 30 minutes prior to the FORTE pass.